RSC Advances

PAPER

View Article Online
View Journal | View Issue

Cite this: *RSC Adv.*, 2026, **16**, 19826

Carbon nanostructure formation over Ni, Co, Fe on γ-Al_2O_3 during low-temperature dry reforming of methane: insights into mechanisms and catalytic behaviour

Artem Kaporov, *[a] Oleksandr Shtyka, [a] Waldemar Maniukiweicz, [a] Jacek Balcerzak, [b] Hanna Kierzkowska-Pawlak, [b] Marcin Kozanecki, [c] Yulia Steksova [d] and Tomasz Maniecki [a]

Received 11th December 2025
Accepted 8th April 2026

DOI: 10.1039/d5ra09618a

rsc.li/rsc-advances

The study presents an investigation of the influence of transition metal phases – Ni, Co, and Fe – on γ-Al_2O_3-supported catalytic systems on catalytic performance and formation of nanostructured carbon allotropes during low-temperature (500–600 °C) dry reforming of methane (DRM). The synthesised catalysts were comprehensively characterised by AAS, BET, BJH, NH_3– and CO_2-TPD, H_2-TPR, *in situ* XPS, and *in situ* XRD. Catalytic performance was evaluated by GC-TCD monitoring of reactant conversion and syngas yield. Carbon products were analysed by TOC, O_2-TPO, Raman spectroscopy, XRD, and SEM-EDX. Ni/γ-Al_2O_3 displayed excellent performance at both temperatures with noticeable formation of filamentous carbon structures. Co/γ-Al_2O_3 exhibited the highest activity along with the greatest carbon deposition with a graphitic morphology. Fe/γ-Al_2O_3 demonstrated marginal catalytic activity and zero carbon formation, associated with its limited reducibility. The study reveals that metal reducibility governs catalytic activity, while metal-specific carbon growth mechanisms determine catalyst stability, providing insights into the rational catalyst design in low-temperature DRM processes.

Introduction

Carbon dioxide reduction by methane, commonly referred to as dry reforming of methane (DRM), is a complex catalytic process ($CH_4 + CO_2 \leftrightarrow 2CO + 2H_2$, $\Delta H^\circ_{298} = +247$ kJ mol^{-1}, $T = 500$–1000 °C) and represents a promising strategy for simultaneous valorisation of two major greenhouse gases – methane (CH_4) and carbon dioxide (CO_2) – which are converted into syngas, a mixture of carbon monoxide (CO) and hydrogen (H_2), a valuable industrial feedstock. The reaction system involves multiple parallel and competing reactions whose outcomes depend on operating conditions and the properties of the catalyst employed.

Among secondary reactions, carbon-forming reactions such as the Boudouard reaction ($2CO \leftrightarrow CO_2 + C$, $\Delta H^\circ_{298} = -172$ kJ mol^{-1}, $T = 400$–600 °C), methane decomposition ($CH_4 \leftrightarrow C + 2H_2$, $\Delta H^\circ_{298} = +75$ kJ mol^{-1}, $T = 600$–700 °C) are particularly concerning due to their role in catalyst deactivation.[1–5] The morphology of the carbon species formed depends heavily on the reaction temperature, with amorphous structures forming at temperatures below 500 °C and well-ordered nanostructures developing above 500 °C.[6–10]

Carbon allotropes formed during the DRM process exhibit diverse structures and properties, ranging from disordered amorphous carbon to highly ordered nanostructured forms (Table 1).[4,11,12] Amorphous carbons usually cause rapid catalyst deactivation by blocking active sites.[13] Carbon nanomaterials – encompassing graphene, carbon nanotubes (CNTs), carbon nanofibers (CNFs), fullerenes, carbon quantum dots (CQDs),

Table 1 Types of carbon structures formed during dry reforming of methane

Carbon structure	Designation	*T*, °C
Amorphous carbon	C_α	250–500
Pyrolytic carbon	C_β	400–600
Filamentous carbon	C_γ	500–700
Graphitic carbon	C_δ	600–900
Carbide-derived carbon	C_ε	700–1000

[a]*Institute of General and Ecological Chemistry, Faculty of Chemistry, Lodz University of Technology, ul. Zeromskiego 116, 90-924 Lodz, Poland. E-mail: artkaporov@gmail.com*

[b]*Department of Chemical and Molecular Engineering, Faculty of Process and Environmental Engineering, Lodz University of Technology, ul. Wolczanska 213, 93-005 Lodz, Poland*

[c]*Department of Molecular Physics, Faculty of Chemistry, Lodz University of Technology, ul. Zeromskiego 116, 90-924 Lodz, Poland*

[d]*The Biorobotics Institute, Scuola Superiore Sant'Anna, Viale Rinaldo Piaggio 34, 56025 Pontedera (PI), Italy*

graphite, *etc.* – possess well-defined crystalline frameworks and can exhibit valuable physicochemical properties.[13,14]

Transition metals from groups 3–12 of the periodic table, in particular nickel (Ni), cobalt (Co), and iron (Fe), are extensively studied as active phases for DRM catalysts due to their favourable combination of activity, availability, and cost-effectiveness. Ni-based catalysts have gained prominence due to their high efficiency in activating both CH_4 and CO_2 molecules.[15–17] Co-based catalysts demonstrate greater oxidation resistance but remain susceptible to carbon deposition, especially through the Boudouard reaction.[18–21] Fe-based catalysts exhibit lower intrinsic activity at moderate temperatures, but possess unique redox characteristics that influence the pathways of carbon formation *via* intermediate compounds in the form of iron carbides (Fe_xC_y); and are known to require temperatures substantially above 600 °C or specialised activation protocols for effective DRM process.[22–26]

Aluminium oxide (Al_2O_3) is widely used as a support material due to its thermal stability, large surface area, and favourable interactions with transition metal phases.[27,28] Alumina provides moderate to strong metal-support interactions, which affect dispersion, particle size, and stability of metal nanoparticles, though these interactions may promote the formation of mixed metal-aluminate compounds.[29–31] Over Al_2O_3-supported catalysts, carbon typically grows by a tip-growth mechanism, where metal particles detach from the support and are carried at the growing ends of carbon filaments.[32,33]

The pronounced variation in the reducibility across Ni, Co, and Fe supported on γ-Al_2O_3 – arising from differences in the strength of the metal-support interaction and the propensity to form thermally stable aluminate phases – makes these three systems a clearly defined comparative set for identifying the role of metal centre density in catalytic activity and carbon formation under low-temperature conditions.

This article provides a comprehensive study of the influence of transition metal phases – Ni-, Co-, and Fe – on γ-Al_2O_3-supported catalytic systems on the formation of nanostructured allotropic forms of carbon and on catalytic activity during low-temperature dry reforming of methane. These systems were selected, spanning the entire range of metal reducibility achievable on γ-Al_2O_3 under identical preparation and activation conditions: from readily and moderately reducible Co and Ni, respectively, to the largely irreducible Fe. This deliberate approach allows the availability of metal centres to be isolated as the governing variable for both catalytic activity and carbon formation, with Fe/γ-Al_2O_3 serving as a mechanistic reference system in which the virtually complete suppression of metallic Fe^0 formation enables a direct verification of the hypothesis that reduced metal sites are a prerequisite for carbon growth during the low-temperature DRM. The study employs a multi-technique analytical approach to establish quantitative relationships between reducibility, active site density, catalytic efficiency, and carbon formation, providing insights into the rational design of catalysts for optimising the low-temperature DRM process, aimed either at the syngas production or the controlled synthesis of nanostructured carbon allotropes.

Results and discussion

Characterisation of the catalytic systems

Physicochemical properties. The textural properties of the studied catalytic systems, including active phase content (w_{AP}), specific surface area (S_{BET}), total pore volume (V_P), and average pore size (D_P), are summarised in Table 2.

The pore size distributions were narrow and unimodal, centred within the mesopore range of 2–4 nm for all three catalysts, consistent with the behaviour of a Type IV N_2 adsorption–desorption isotherm with H2-type hysteresis, characteristic of γ-Al_2O_3-supported systems.[27,28] The observed differences in SBET and VP values among the catalytic systems are attributed to the extent of pore occlusion by metal oxide species deposited during impregnation. Ni/γ-Al_2O_3 demonstrated the lowest S_{BET} of 88 $m^2\ g^{-1}$ and V_P of 0.17 $cm^3\ g^{-1}$, reflecting a more extensive coverage of the alumina surface by the nickel oxide phase, which is consistent with the highest total acidity (0.77 mmol g^{-1}, Table 3), arising from the strong interaction of Ni^{2+} ions with the γ-Al_2O_3 surface, generating new acid sites.[34] Conversely, Fe/γ-Al_2O_3 retained the largest S_{BET} of 102 $m^2\ g^{-1}$ and V_P of 0.22 $cm^3\ g^{-1}$, associated with the predominantly lattice-incorporated speciation of Fe suggested by its lowest acidity (0.49 mmol g^{-1}) and highest basicity (3.74 mmol g^{-1}, Table 3), wherein iron substitutes into the alumina framework rather than forming discrete surface oxide clusters that would partially block the pore network.[35] The preserved mesoporous architecture across all systems ensures efficient intraparticle diffusion of reactants and products, which is particularly essential during the low-temperature DRM process.[16,24,34,36]

The acid–base properties of the studied catalytic systems, such as concentration and distribution of acid and basic centres, are shown in Table 3.

Ni/γ-Al_2O_3 exhibited the highest total acidity (0.77 mmol g^{-1}) with a balanced distribution between weak (44%), medium (32%), and strong (23%) acid sites, as well as the lowest total basicity (1.89 mmol), mainly composed of medium (47%) and strong (46%) basic sites. This distribution promotes the activation of both CH_4 and CO_2, which is essential for effective DRM performance.[37]

Co/γ-Al_2O_3 displayed moderate acidity (0.61 mmol g^{-1}) with a nearly equal distribution between weak (42%) and medium (41%) acid sites, as well as average basicity (2.54 mmol g^{-1}) primarily associated with medium-strength basic sites (76%).

Table 2 Textural properties of the studied catalytic systems

Sample	w_{AP}, % w/w	S_{BET}, $m^2\ g^{-1}$	V_P, $cm^3\ g^{-1}$	D_P, nm
Ni/γ-Al_2O_3	18.6	88	0.17	2.7
Co/γ-Al_2O_3	19.9	93	0.18	2.8
Fe/γ-Al_2O_3	21.0	102	0.22	3.1

Table 3 Concentration of acid and basic centres in the studied catalytic systems

	Acidic sites, mmol g^{-1}			Basic sites, mmol g^{-1}		
Sample	Weak 100–300 °C	Medium 300–450 °C	Strong 450–600 °C	Weak 100–300 °C	Medium 300–450 °C	Strong 450–600 °C
Ni/γ-Al_2O_3	0.34	0.25	0.18	0.13	0.89	0.87
Co/γ-Al_2O_3	0.26	0.25	0.10	0.14	1.94	0.47
Fe/γ-Al_2O_3	0.23	0.19	0.06	0.52	2.12	1.10

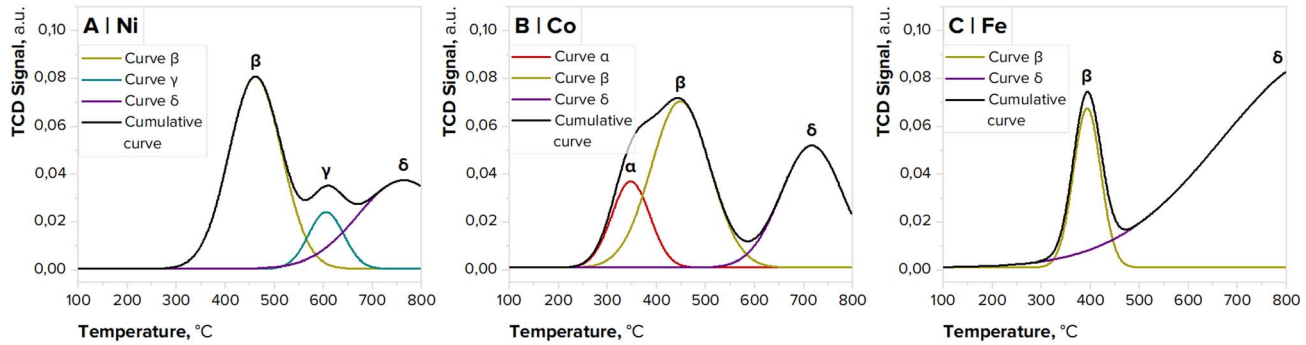

Fig. 1 H_2-TPR profiles of Ni/γ-Al_2O_3 (A), Co/γ-Al_2O_3 (B), and Fe/γ-Al_2O_3 (C).

Such moderate acidity and strong basicity can considerably influence the DRM process pathways, enhancing CO_2 activation.[38]

Fe/γ-Al_2O_3 demonstrated the lowest acidity (0.49 mmol g^{-1}) with pronounced weak (48%) and medium (39%) acid sites; however, the highest basicity (3.74 mmol g^{-1}), expressed mostly in medium (57%) basic sites. This pronounced basic character indicates excellent CO_2 adsorption capacity but potentially limited CH_4 activation due to its low acidity.[35]

Reducibility of the catalytic systems. The results of H_2-TPR analysis of the studied catalytic systems are demonstrated in Fig. 1 and Table 4.

Ni/γ-Al_2O_3 (Fig. 1A) exhibited three distinct reduction peaks: **β** at 460 °C corresponded to the reduction of NiO species with weak support interaction; **γ** at 610 °C attributed to the reduction of NiO species moderately interacting with the γ-Al_2O_3; **δ** at 760 °C assigned to the reduction of strongly bound $NiAl_2O_4$ structures.[16,39–41] The multiple peak profile indicates a heterogeneous distribution of Ni species with varying ease of reduction.

Co/γ-Al_2O_3 (Fig. 1B) demonstrated a similar three-peak profile: **α** at 350 °C associated with the two-step reduction of Co_3O_4 to CoO and Co^0; **β** at 450 °C ascribed to the reduction of CoO species weakly interacting with the support; **δ** at 720 °C related to the reduction of $CoAl_2O_4$ species.[42–45] The presence of the peak **α** and the absence of the peak **γ** distinguished Co/γ-Al_2O_3 from Ni/γ-Al_2O_3, suggesting the existence of easily reducible Co_3O_4 crystallites and the lack of strongly bound Co–Al_2O_3 species.

Fe/γ-Al_2O_3 (Fig. 1C) showed a markedly different reduction profile with only two peaks: **β** at 390 °C associated with the partial reduction of Fe_2O_3 to Fe_3O_4 and FeO; **δ** at 890 °C attributed to the reduction of $FeAl_2O_4$ species.[24,46] The exceptionally high temperature and largest area (48.4) of peak **δ** suggest that *ca.* 91% of Fe species exist in the form of strongly bound aluminates, severely limiting the catalyst reducibility and significantly impacting the catalytic activity in the DRM process.

The results of *in situ* XPS analysis of the surface reduction of the studied catalytic systems are given in Fig. 2–4.

The Ni/γ-Al_2O_3 spectra in the $Ni2p_{3/2}$ region (Fig. 2) revealed significant changes upon reduction. Before reduction (Fig. 2A), the spectrum was dominated by the NiO peak (854.4 eV, peak area 60.3%) with the typical satellite peak (860.6 eV, 39.7%).[39,47,48] After reduction (Fig. 2B), the profile showed the metallic Ni^0 peak (852.6 eV, 70.4%) as well as the $NiAl_2O_4$ peak (856.5 eV, 29.6%), suggesting partial reduction of the supported nickel species. The incomplete reduction (*ca.* 70% of reduced Ni^0 species, according to peak area analysis) aligns with the significant fraction of difficult-to-reduce NiO and $NiAl_2O_4$ species observed in the H_2–TPR profile (peaks **γ** and **δ**, Fig. 1A).[49,50]

The Co/γ-Al_2O_3 spectra in the $Co2p_{3/2}$ region (Fig. 3) displayed more pronounced changes upon reduction compared to

Table 4 H_2-TPR data for the studied catalytic systems

	Peak α		Peak β		Peak γ		Peak δ	
Sample	*T*, °C	Area	*T*, °C	Area	*T*, °C	Area	*T*, °C	Area
Ni/γ-Al_2O_3	—	—	460	10.8	610	2.1	760	8.7
Co/γ-Al_2O_3	350	3.5	450	10.4	—	—	720	8.0
Fe/γ-Al_2O_3	—	—	390	4.6	—	—	890	48.4

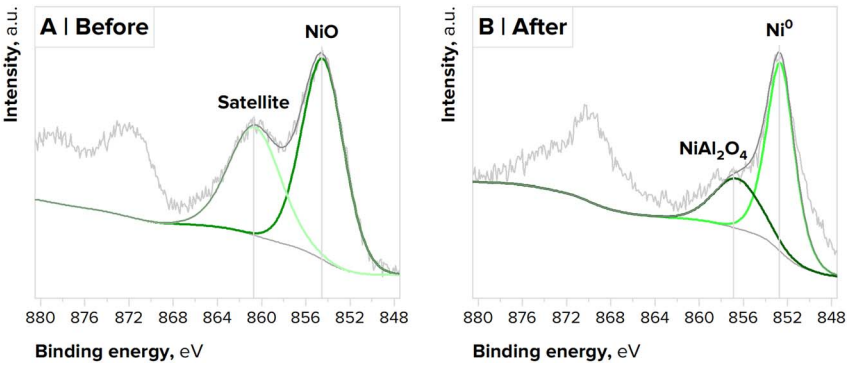

Fig. 2 XPS spectra of Ni/γ-Al_2O_3 in the Ni2$p_{3/2}$ region before (A) and after reduction (B).

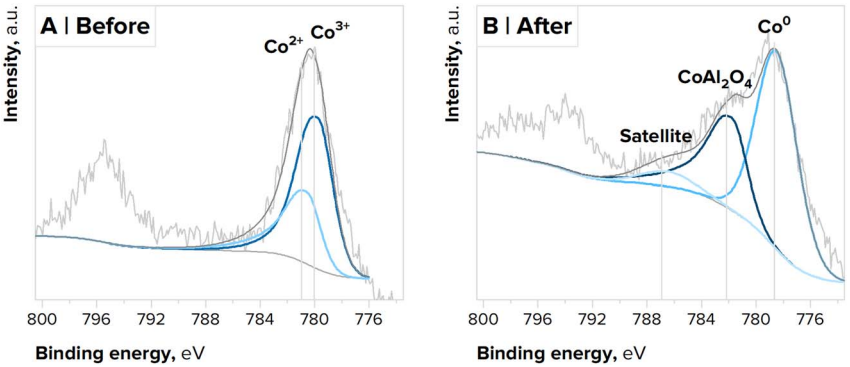

Fig. 3 XPS spectra of Co/γ-Al_2O_3 in the Co2$p_{3/2}$ region before (A) and after reduction (B).

Ni/γ-Al_2O_3. Before reduction (Fig. 3A), the spectrum was dominated by the Co^{3+} peak (779.8 eV, peak area 66%) and the Co^{2+} peak (780.6 eV, 34%), representing Co_3O_4 species in a ratio of 66%:34%, respectively.[51] After reduction (Fig. 3B), the profile showed the emergence of the Co^0 peak (778.5 eV, 61.2%) with the typical satellite peak (786.5 eV, 6.0%) as well as the $CoAl_2O_4$ peak (781.8 eV, 32.8%).[52] The partial reduction (*ca.* 60% of reduced Co^0 species, according to peak area analysis), as in the case of Ni/γ-Al_2O_3, reflects the presence of easily reducible Co species alongside the difficult-to-reduce $CoAl_2O_4$ species identified in the H_2-TPR profile (peaks α and δ, Fig. 1B).[43]

The Fe/γ-Al_2O_3 spectra in the Fe2$p_{3/2}$ region (Fig. 4) exhibited the most complex features among the studied catalysts. Before reduction (Fig. 4A), the spectrum was governed by the Fe^{3+} peak (710.8 eV, peak area 67.6%) and the Fe^{2+} peak (709.2 eV, 32.4%), representing Fe_3O_4 species in a ratio of 67.6%:32.4%, respectively. After reduction (Fig. 4B), the profile revealed the Fe^0 peak (707.0 eV, 21.0%) with the prevailing Fe_2O_3 and FeO peaks remaining (710.9 eV, 41.9%; 709.2 eV, 37.1%). The minimal catalyst reduction compared to other systems (*ca.* 20% of reduced Fe^0 species, according to peak area analysis) coincides with the complete predominance of firmly bound, difficult-to-

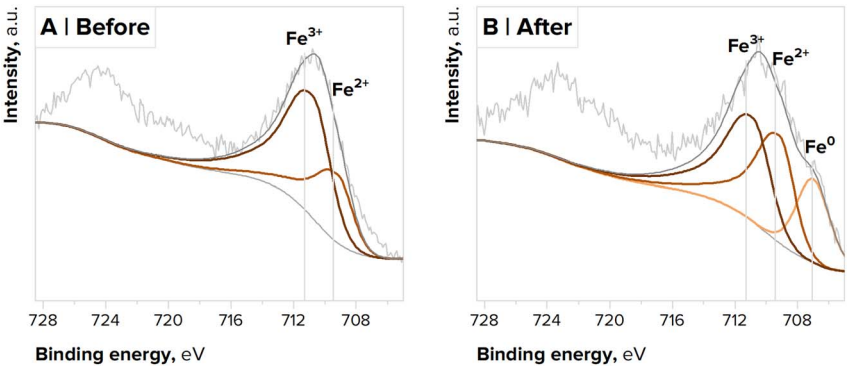

Fig. 4 XPS spectra of Fe/γ-Al_2O_3 in the Fe2$p_{3/2}$ region before (A) and after reduction (B).

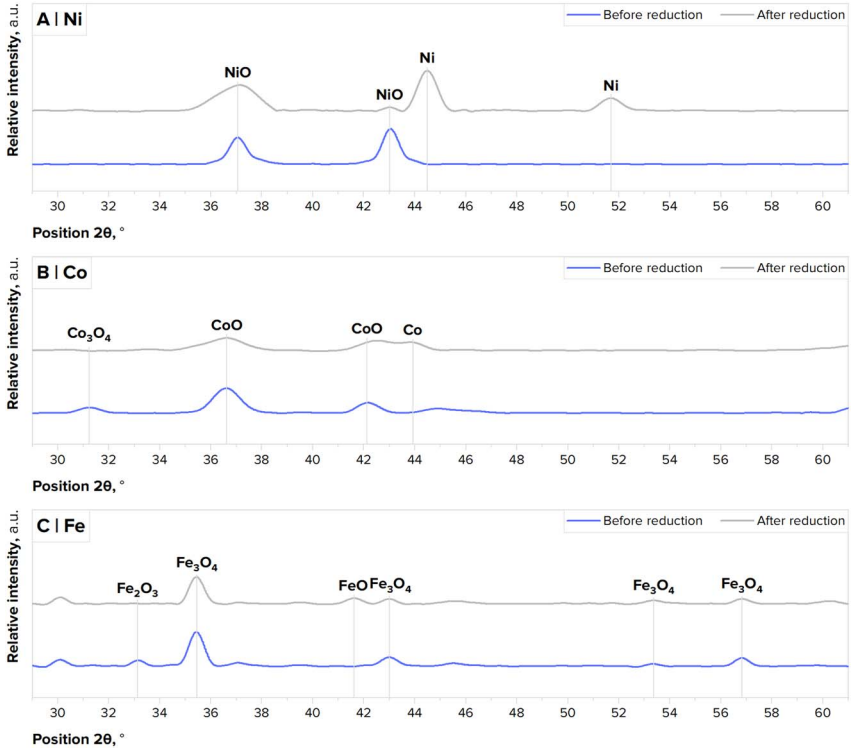

Fig. 5 *In situ* XRD patterns of Ni/γ-Al_2O_3 (A), Co/γ-Al_2O_3 (B), and Fe/γ-Al_2O_3 (C) before and after reduction.

reduce Fe species, as evidenced by the H_2-TPR data (peak δ with *ca.* 91% of peak area, Fig. 1C). The coexistence of Fe^{2+}, Fe^{3+}, and Fe^0 species after reduction may have crucial implications for the Fe/γ-Al_2O_3 activity in the DRM process.

The results of *in situ* XRD analysis of the bulk reduction of the studied catalytic systems are presented in Fig. 5.

The Ni/γ-Al_2O_3 pattern (Fig. 5A) exhibited significant structural changes upon reduction. Before reduction, NiO peaks were observed at 2θ of 37° and 43°. After reduction, the diffractogram showed Ni^0 peaks at 2θ of 44° and 52° with a crystallite size of 28 nm, while the intensity of the NiO peaks decreased substantially, confirming the *in situ* XPS data (*ca.* 70% of reduced Ni^0 species, Fig. 2). The sharp and intense Ni^0 peaks imply the formation of relatively large, well-crystallised metal particles, which may influence both catalytic activity and carbon deposition in the DRM process.[53]

The Co/γ-Al_2O_3 pattern (Fig. 5B) displayed more subtle transformations compared to Ni/γ-Al_2O_3. Before reduction, CoO peaks associated with CoO were noted at 2θ of 31°, 37°, and 42°. After reduction, the Co^0 peak appeared at 2θ of 44°, while the intensity of CoO peaks diminished but remained prominent, correlating with the *in situ* XPS data (*ca.* 60% of reduced Co^0 species, Fig. 3). The Co^0 peak was less intense and broader than its Ni^0 counterpart, suggesting smaller crystallite sizes of 6 nm, which may affect carbon formation mechanisms due to the tendency of smaller Co particles to exhibit lower methane decomposition rates.[34]

The Fe/γ-Al_2O_3 pattern (Fig. 5C) revealed the most complex phase behaviour. Before reduction, the diffractogram showed multiple oxide phases: Fe_3O_4 at 2θ of 30°, 35°, 43°, 53°, and 57°, as well as Fe_2O_3 at 2θ of 33°. After reduction, the profile remained essentially unchanged, with no obvious evidence of Fe^0 peaks, but with the weak FeO peak at 2θ of 42°, indicating an incomplete stepwise reduction. These observations are supported by the partial reduction, according to the *in situ* XPS data (*ca.* 20% of reduced Fe^0 species, Fig. 4). The absence of Fe^0 peaks in the pattern suggests that the reduced Fe^0 species exist either as amorphous phases or as ultrafine crystallites below the XRD detection limit.[26]

Catalytic measurements

The calculated thermodynamic parameters for dry reforming of methane, as well as the Boudouard reaction and methane decomposition at 500 °C and 600 °C, including the standard enthalpy change ($\Delta H°$), standard entropy change ($\Delta S°$), standard Gibbs free energy change ($\Delta G°$), and equilibrium constant (K), are summarised in Table 5.

Dry reforming of methane is a strongly endothermic reaction with a large positive entropy change ($\Delta H° = +247.4$ kJ mol^{-1}, $\Delta S° = +256.7$ J mol^{-1} K^{-1}), reflecting an increase in the molar quantity from two reactant molecules to four product molecules. At 500 °C, the Gibbs free energy change remains substantially positive ($\Delta G° = +48.9$ kJ mol^{-1}), yielding an equilibrium constant of only 4.94×10^{-4}, indicating that the reaction is thermodynamically unfavourable under these conditions. However, at 600 °C, the Gibbs free energy change increases to +23.3 kJ mol^{-1} with a corresponding increase in the equilibrium constant to 4.1×10^{-2}, which reveals a pronounced

Table 5 Thermodynamic parameters for dry reforming of methane and carbon-forming side reactions

Reaction	T, °C	$\Delta H°$, kJ mol^{-1}	$\Delta S°$, J mol^{-1} K^{-1}	$\Delta G°$, kJ mol^{-1}	K
Dry reforming of methane	500	+247.4	+256.7	+48.9	4.94×10^{-4}
	600	+247.4	+256.7	+23.3	4.1×10^{-2}
Boudouard reaction	500	−172.5	−175.9	−36.5	293
	600	−172.5	−175.9	−18.9	13.5
Methane decomposition	500	+74.9	+80.8	+12.4	1.4×10^{-1}
	600	+74.9	+80.8	+4.3	5.5×10^{-1}

temperature sensitivity characteristic of an endothermic process.

The Boudouard reaction is an exothermic reaction with a negative entropy change ($\Delta H° = -172.5$ kJ mol^{-1}, $\Delta S° = -175.9$ J mol^{-1} K^{-1}) due to a decrease in the molar quantity in the gas phase. This reaction is thermodynamically favourable at both temperatures, with the Gibbs free energy change and the equilibrium constant at 500 °C being −36.5 kJ mol^{-1} and 293, respectively, and at 600 °C being −18.9 kJ mol^{-1} and 13.5, respectively. A considerable decrease in the magnitude of both parameters with increasing temperature is characteristic of exothermic reactions following the Van't Hoff equation. Nevertheless, even at 600 °C, the equilibrium constant remains well above unity, indicating that carbon deposition *via* the Boudouard reaction mechanism continues to be thermodynamically driven.

Methane decomposition is a moderately endothermic reaction with a positive entropy change ($\Delta H° = +74.9$ kJ mol^{-1}, $\Delta S° = +80.8$ J mol^{-1} K), resulting in the formation of two H_2 molecules from one CH_4 molecule. At 500 °C, the reaction remains slightly unfavourable with the Gibbs free energy change and equilibrium constant of +12.4 kJ mol^{-1} and 1.4×10^{-1}, respectively, but at 600 °C it approaches thermodynamic neutrality (+4.3 kJ mol^{-1} and 5.5×10^{-1}, respectively). This temperature dependence suggests that methane decomposition becomes increasingly significant at higher temperatures within the DRM operating window.

The conversions of CO_2 and CH_4 over the studied catalytic systems during the DRM process are shown in Fig. 6.

At 500 °C (Fig. 6A), Co/γ-Al_2O_3 displayed the highest initial CH_4 conversion of 81%, followed by Ni/γ-Al_2O_3 of 68%, while CO_2 conversions were consistently lower: 60% over Co/γ-Al_2O_3 and 46% over Ni/γ-Al_2O_3. At the end of the catalytic measurements, the conversions of both gases declined relatively insignificantly: to 63% for CH_4 and 43% for CO_2 over Ni/γ-Al_2O_3; to 76% for CH_4 and 59% for CO_2 over Co/γ-Al_2O_3. The higher conversion of CH_4 compared to CO_2 suggests that methane decomposition occurs as a parallel reaction alongside the primary DRM reaction, which is also corroborated by the CH_4/CO_2 conversion ratio of 1.3–1.6.

At 600 °C (Fig. 6B), the activity of both catalytic systems increased significantly – conversions of CH_4 and CO_2 over Ni/γ-Al_2O_3 reached 80% and 64%, respectively, with a slight decrease to 76% for CH_4 and 60% for CO_2; whereas Co/γ-Al_2O_3 maintained the highest conversion of CH_4 at 80% and CO_2 at 69%, but showed a progressive deactivation, achieving 73% for CH_4 and 57% for CO_2 at the end. The CH_4/CO_2 conversion ratio for each catalyst decreased, opposed to the catalytic measurements at 500 °C, and is 1.2–1.4 with a shift towards the primary DRM reaction, proving the thermally activated nature of Ni/γ-Al_2O_3 and Co/γ-Al_2O_3, where higher temperatures contribute to the activation of both reactants.[54,55] This superior performance at both temperatures is probably attributed to the large amount of reduced Ni^0 and Co^0 species in the system structures after reduction (*ca.* 70% and 60%, respectively), as confirmed by the *in situ* XPS (Fig. 2 and 3) and *in situ* XRD (Fig. 5A and B) data.

Conversely, Fe/γ-Al_2O_3 revealed markedly lower catalytic activity at 500 °C (Fig. 6A): the initial conversion of CH_4 was 8%, and that of CO_2 was 6%, rapidly declining to 2% and 3%, respectively. At 600 °C (Fig. 6B), the conversion of both gases increased marginally but remained inferior: 10% for CH_4 and 11% for CO_2, decreasing to 6% and 7%, respectively. The almost

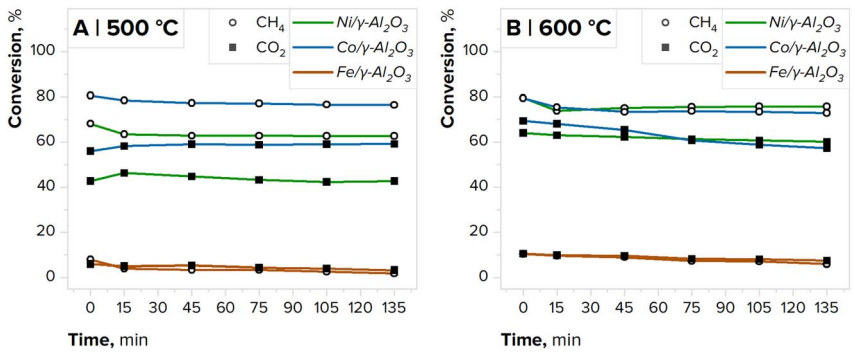

Fig. 6 Conversion of CO_2 and CH_4 over the studied catalytic systems during the catalytic measurements at 500 °C (A) and 600 °C (B).

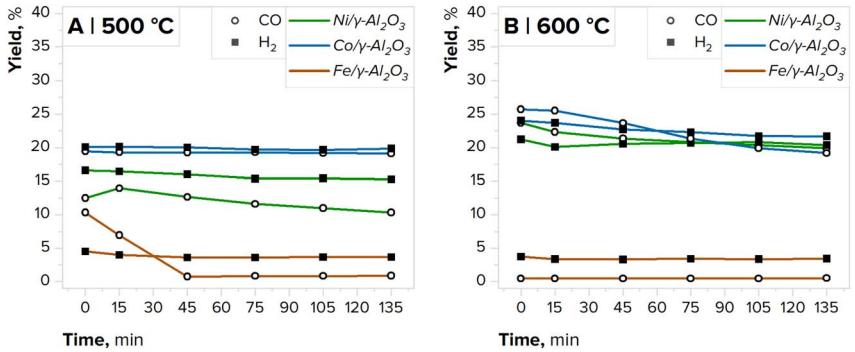

Fig. 7 Yield of CO and H_2 over the studied catalytic systems during the catalytic measurements at 500 °C (A) and 600 °C (B).

complete absence of activity is directly driven by the incomplete reduction of Fe/γ-Al_2O_3, expressed in the minimal content of reduced Fe^0 species (*ca.* 20%, Fig. 4), as well as the prevalence of difficult-to-reduce oxide and aluminate forms in the catalyst structure (Fig. 1C and 5C). Since oxide phases are catalytically incapable of efficiently activating both CH_4 and CO_2, the minimal observed conversion most likely reflects background thermal reactions rather than genuine catalytic activity.[35,56] The behaviour of Fe/γ-Al_2O_3 under the studied conditions is consistent with its severely limited reducibility, as determined by H_2-TPR (peak δ, Fig. 1C) and *in situ* XPS (*ca.* 20% of reduced Fe^0, Fig. 4), as well as with the fact that Fe-based DRM catalysts require temperatures substantially exceeding 600 °C to form a sufficient number of metallic or carbide active sites.[22–25,36] Within the present study, the near-complete inactivity of Fe/γ-Al_2O_3 provides a critical mechanistic reference, since it demonstrates that the catalytic activity observed for Ni/γ-Al_2O_3 and Co/γ-Al_2O_3 is inextricably linked to the presence of metallic surface sites, rather than being a consequence of purely thermal or support-mediated processes.

The yields of CO and H_2 over the studied catalytic systems during the DRM process are demonstrated in Fig. 7.

At 500 °C (Fig. 7A), both Ni/γ-Al_2O_3 and Co/γ-Al_2O_3 exhibited moderate to high syngas yield: 14% for CO and 17% for H_2 over Ni/γ-Al_2O_3; 20% for both CO and H_2 over Co/γ-Al_2O_3. At the end of the catalytic measurements, a relatively minor decline in yield was observed for Ni/γ-Al_2O_3, amounting to 10% for CO and 15% for H_2, whereas Co/γ-Al_2O_3 maintained the same level of 20% for both CO and H_2.

At 600 °C (Fig. 7B), yields increased marginally, achieving 24% for CO and 21% for H_2, gradually decreasing to 20% for both gases over Ni/γ-Al_2O_3, and reaching 26% for CO and 24% for H_2, declining to 19% and 22%, respectively, over Co/γ-Al_2O_3. The relatively near-stoichiometric H_2/CO ratio at each temperature reflects the trade-off between enhanced reaction kinetics and accelerated catalytic deactivation (Fig. 6).

Contrary to other systems, Fe/γ-Al_2O_3 showed negligible catalytic efficiency for syngas production. At 500 °C (Fig. 7A), the initial CO and H_2 yields were 10% and 5%, respectively, rapidly decreasing to 1% for CO and 4% for H_2. At 600 °C (Fig. 7B), the yields remained insignificant, with initial values of 1% for CO and 4% for H_2, showing no substantial changes during the catalytic measurements.

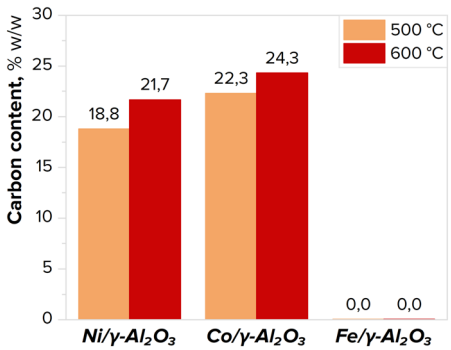

Fig. 8 Content of the carbon species in the samples after the catalytic measurements at 500 °C and 600 °C.

Characterisation of the products

Analysis of carbon species. The results of TOC analysis of the carbon allotropes formed over the studied catalytic systems after the catalytic measurements are shown in Fig. 8.

Ni/γ-Al_2O_3 exhibited moderate carbon formation, with 18.8% w/w at 500 °C and 21.7% w/w at 600 °C. The modest uptick in the carbon content with rising temperature suggests both enhanced kinetics of methane decomposition and concurrent carbon gasification at elevated temperatures, as evidenced by the increase in CH_4 and CO_2 conversion and CO yield at 600 °C, opposed to 500 °C (Fig. 6 and 7).

Co/γ-Al_2O_3 displayed the highest carbon accumulation among the studied systems, with 22.3% w/w at 500 °C and 24.3% w/w at 600 °C. This enhanced carbon yield correlates with the superior CH_4 activation ability at both 500 °C and 600 °C, where it even surpasses the performance of Ni/γ-Al_2O_3 (Fig. 6), while the modest temperature effect indicates approaching saturation caused by more complex mechanisms of carbon formation compared to those over Ni/γ-Al_2O_3.[34]

Fe/γ-Al_2O_3 demonstrated no detectable carbon formation at either 500 °C or 600 °C. These observations are directly intertwined with the negligible catalytic activity, presumably associated with the background thermal processes rather than the intended reactions (Fig. 6). As foreseen, such absence of

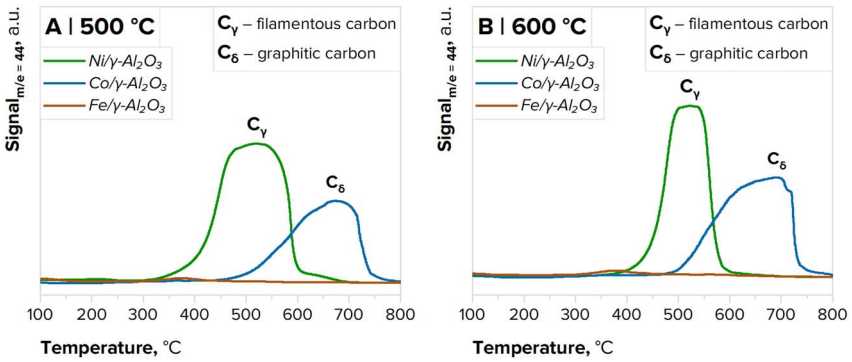

Fig. 9 O_2-TPO patterns of the samples after the catalytic measurements at 500 °C (A) and 600 °C (B).

performance over Fe/γ-Al_2O_3 has a direct bearing on the partial reduction of Fe/γ-Al_2O_3, as outlined by the *in situ* reduction studies (*ca.* 20% of reduced Fe^0 species, Fig. 4 and 5C). The absence of any detectable carbon deposition over Fe/γ-Al_2O_3 directly indicates that the formation of nanostructured carbon allotropes during the low-temperature DRM is contingent on the availability of metallic surface centres. This finding confirmed the mechanistic significance of the Fe/γ-Al_2O_3 system within the scope of this study, as its inclusion enables the necessary condition for carbon growth to be defined experimentally, against which the behaviour of the catalytically active Ni- and Co-based systems can be quantitatively interpreted.

The results of O_2-TPO analysis of the carbon allotropes formed over the studied catalytic systems after the catalytic measurements are presented in Fig. 9.

The Ni/γ-Al_2O_3 profiles revealed the single dominant peak $\mathbf{C_\gamma}$ (500 °C) at both temperatures. This oxidation temperature is characteristic of filamentous carbon (CNTs of CNFs) with a moderate degree of graphitisation.[54] The well-defined nature of the peak and its constant position regardless of temperature suggest that the fundamental structure of the deposited carbon is homogeneous and remains consistent across the entire temperature range. The tip-growth mechanism of carbon formation over Ni/γ-Al_2O_3 is supported by convergent evidence from multiple characterisation techniques. The *ca.* 70% of reduced Ni^0, determined by *in situ* XPS (Fig. 2), provides sufficient density of metallic ensemble sites required for CH_4 dissociation and subsequent carbon dissolution into the metal bulk.[57] The substantially higher CH_4 conversion relative to CO_2 (CH_4/CO_2 ratio of 1.3–1.6, Fig. 6) indicates a significant contribution of methane decomposition as a parallel carbon-forming pathway alongside the primary DRM reaction, consistent with the thermodynamic feasibility of this reaction at 500–600 °C (Table 5). The moderate total carbon content of 18.8–21.7% w/w (Fig. 8) reflects the combined effect of carbon accumulation *via* both the Boudouard reaction and methane decomposition, which are thermodynamically favourable under the studied conditions (Table 5), with the metallic Ni^0 sites serving as the locus for the carbon nucleation and growth.[57]

The Co/γ-Al_2O_3 profiles displayed a distinctly different pattern, with the single peak $\mathbf{C_\delta}$ (650–700 °C) at both temperatures, indicating the presence of carbon species with more pronounced graphitic character and enhanced thermal stability.[58] The surface diffusion and nucleation mechanism of carbon formation over Co/γ-Al_2O_3 is supported by the following evidence obtained. The *ca.* 60% of reduced Co^0 (Fig. 3), combined with the stronger metal–support interaction manifested as the $CoAl_2O_4$ species identified by H_2–TPR (peak δ, Fig. 1B) and *in situ* XPS (Fig. 3B), suggest a greater tendency of Co particles to remain anchored to the alumina surface compared to Ni, thereby favouring carbon growth controlled by surface diffusion rather than the dissolution-precipitation pathway.[34,59] The smaller Co^0 crystallite size of 6 nm observed

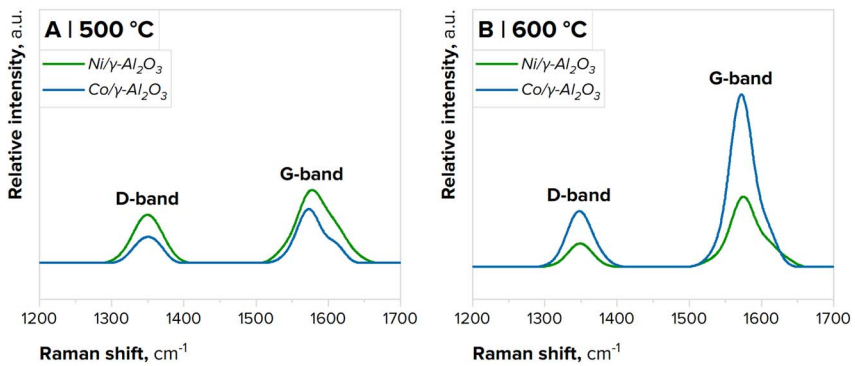

Fig. 10 Raman spectra of the samples after the catalytic measurements at 500 °C (A) and 600 °C (B).

Table 6 Raman spectroscopy data for the studied catalytic systems

Catalyst	T, °C	Intensity ratio (I_D/I_G)	D-band peak width (W_D), cm^{-1}	G-band peak width (W_G), cm^{-1}
Ni/γ-Al_2O_3	500	0.80	49.4	53.9
	600	0.41	37.5	43.4
Co/γ-Al_2O_3	500	0.48	40.7	48.3
	600	0.47	35.8	46.1

after reduction by *in situ* XRD (Fig. 5B), compared to 28 nm for Ni^0, is consistent with this behaviour, as smaller, surface-anchored particles promote lateral carbon nucleation rather than filament extrusion.[34] The highest carbon accumulation among the studied systems (22.3–24.3% w/w, Fig. 8), combined with the highest initial CH_4 conversion (81% at 500 °C, Fig. 6), reflects the superior CH_4 activation capacity of Co and the efficient channelling of dissociated carbon into thermally stable graphitic structures. The progressive deactivation of Co/γ-Al_2O_3 at 600 °C (CH_4 conversion declining from 80% to 73% over 150 min, Fig. 6) is consistent with the gradual coating of active Co^0 sites by the growing layer of graphitic carbon, which is thermodynamically stable at the studied temperatures (Table 5).

The Fe/γ-Al_2O_3 profiles did not display any noticeable peaks across the entire temperature range, confirming previous findings that a small amount of reduced Fe^0 species (*ca.* 20%, Fig. 4) and the predominance of difficult-to-reduce species (peak δ with *ca.* 91% of peak area, Fig. 1C and 5C) suppress both carbon-forming reactions and the primary DRM reaction, resulting in marginal catalytic activity (Fig. 6 and 7).

The results of Raman spectroscopy of the carbon allotropes formed over the studied catalytic systems after the catalytic measurements are presented in Fig. 10 and Table 6.

The Ni/γ-Al_2O_3 spectra showed two distinct characteristic bands: the D-band at 1350 cm^{-1} (disorder band, associated with structural defects in carbon materials) and the G-band at 1576 cm^{-1} (graphitic band, related to the in-plane vibrational mode of sp^2-bonded carbon atoms in ordered graphitic structures).[60] The decrease in the relative intensity ratio (I_D/I_G) from 0.80 at 500 °C to 0.41 at 600 °C, as well as the narrowing of the peak widths (W_D: from 49.4 cm^{-1} at 500 °C to 37.5 cm^{-1} at 600 °C; W_G: from 53.9 to 43.4 cm^{-1}, respectively) indicate a significant reduction in structural defects in the formed carbon allotropes and enhanced graphitisation, which is also consistent with the sharper oxidation peak $\mathbf{C}_\gamma$ at 600 °C compared to 500 °C (Fig. 9).[61] The temperature-dependent decrease in the I_D/I_G ratio from 0.80 to 0.41, combined with the constant position of the oxidation peak $\mathbf{C}_\gamma$ (Fig. 9), indicates that the graphitisation proceeds within the same structural type of carbon – filamentous – rather than reflecting a transition between carbon allotropes. This is consistent with the tip-growth mechanism proposed on the basis of the results of *in situ* XPS, H_2-TPR, and GC-TCD, whereby an increase in temperature enhances the ordering of graphitic planes within the walls of the growing filaments without altering the fundamental growth regime.

The Co/γ-Al_2O_3 spectra also displayed D- and G-bands at 1349 cm^{-1} and 1573 cm^{-1}, respectively. The I_D/I_G ratio is consistently low with minimal temperature dependence – 0.48 at 500 °C and 600 °C – confirming the inherently graphitic character of the carbon allotropes formed, which is aligned with the O_2–TPO results (Fig. 9), showing a higher oxidation temperature (peak $\mathbf{C}_\delta$ at 650–700 °C). The peak widths decreased marginally with the temperature growth (W_D: from 40.7 cm^{-1} at 500 °C to 35.8 cm^{-1} at 600 °C; W_G: from 48.3 cm^{-1} to 46.1 cm^{-1}, respectively), suggesting a modest improvement in the structure of the carbon allotropes, which have graphitic nature throughout the entire temperature range, reflecting the early discussed behaviour of Co/γ-Al_2O_3 towards the formation of such carbon. The temperature independence of the I_D/I_G ratio (0.48 at both 500 °C and 600 °C) stands in sharp contrast to the pronounced temperature dependence observed for Ni/γ-Al_2O_3 and is consistent with a growth mechanism governed by surface diffusion, in which the graphitic ordering is determined primarily by the intrinsic properties of the Co^0 surface rather than by the reaction temperature. This interpretation aligns with the smaller size of Co^0 crystallite (6 nm, Fig. 5B) and stronger metal-support interaction (Fig. 1B and 3B), established prior to the catalytic measurements, as well as with the higher oxidation temperature of peak $\mathbf{C}_\delta$ (Fig. 9), indicating a more ordered carbon structure than that produced over Ni/γ-Al_2O_3.

Table 7 Carbon balance for the studied catalytic systems at 500 °C and 600 °C

Catalyst	T, °C	X_{CH_4}, %	X_{CO_2}, %	Y_{CO}, %	Y_{H_2}, %	$r_{H_2/CO}$	n_C^{in}, mmol	n_C^{out}, mmol	CB, %	CDE, %
Ni/γ-Al_2O_3	500	63.78	43.69	12.00	15.85	1.33	167.31	107.42	64.21	5.76
	600	75.93	61.93	21.41	20.62	0.97	167.31	99.38	59.40	6.90
Co/γ-Al_2O_3	500	77.75	58.42	19.26	19.92	1.03	167.31	97.62	58.35	7.14
	600	74.72	63.32	22.56	22.69	1.01	167.31	103.52	61.87	7.99
Fe/γ-Al_2O_3	500	3.88	4.67	3.43	3.84	3.08	167.31	164.35	98.23	0.00
	600	8.15	8.98	0.48	3.44	7.15	167.31	154.40	92.28	0.00

Raman spectra for Fe/γ-Al_2O_3 are not presented, as no detectable carbon species were observed, agreeing with the TOC (Fig. 8) and O_2-TPO (Fig. 9) analyses, both of which confirmed the absence of carbon deposition over this system under the studied conditions.

The results of the carbon balance analysis, quantifying the distribution of inlet carbon between the gas phase and solid deposits over the studied catalytic systems at 500 °C and 600 °C, including the conversion of CH_4 and CO_2 (X_{CH_4}, X_{CO_2}), the yield of CO and H_2 (Y_{CO}, Y_{H2}), the H_2/CO ratio ($r_{H2/CO}$), and the amount of the inlet gaseous carbon and the outlet solid and gaseous carbon (n_C^{in}, n_C^{out}), are summarised in Table 7. The detailed data for each of the studied catalysts are provided in the SI (Tables S1–S6).

The carbon balance closure of 58–64% for Ni/γ-Al_2O_3 and Co/γ-Al_2O_3 is below the ideal value of 100% and requires explicit consideration. This gap is explainable by carbon deposits accumulated on the inner walls of the quartz reactor tube, in the gas supply lines, and on the downstream fittings, which were not collected or subjected to TOC analysis; only the catalyst bed (0.50 g) was characterised. Carbon deposition on reactor equipment is a recognised phenomenon in fixed-bed DRM experiments conducted under conditions of intense carbon formation, and the magnitude of the deficit observed here is consistent with the thermodynamic driving force for both the Boudouard reaction and methane decomposition, as confirmed under the studied conditions (Table 5).[4,5,19,20] The systematic nature of this effect is directly evidenced by the correlation between catalytic activity and the extent of the carbon balance shortage. Thus, Ni/γ-Al_2O_3 and Co/γ-Al_2O_3, which display a high conversion of CH_4 (Fig. 6) and confirmed formation of solid carbon species by TOC (Fig. 8), show CB of 58–64%, whereas Fe/γ-Al_2O_3, for which TOC analysis revealed the complete absence of carbon deposition, demonstrates CB of 92–98%. The near-complete carbon closure for Fe/γ-Al_2O_3 – a system with negligible catalytic activity established by GC–TCD (Fig. 6 and 7) and minimal metal centre density according to H_2-TPR (Fig. 1C) and *in situ* XPS (Fig. 4) – validates the reliability of the gas-phase analytical methodology and implies that the lower balance closure values for Ni- and Co-based systems reflect the genuine redistribution of carbon to reactor surfaces rather than instrumental errors. The carbon deposition efficiency, quantifying the fraction of inlet carbon immobilised on the catalyst bed as measured by TOC, is reported alongside the carbon balance closure as a complementary metric of carbon utilisation.

Crystallinity and phase composition. The results of XRD analysis of the samples after reduction and the catalytic measurements at 500 °C and 600 °C, revealing phase composition and crystallinity, are shown in Fig. 11 and Table 8.

The Ni/γ-Al_2O_3 pattern (Fig. 11A) after reduction displayed characteristic Ni^0 peaks at 2θ of 44°, 52°, and 76°, NiO at 2θ of 37°, γ-Al_2O_3 at 2θ of 67°, as well as an initial crystallite size of 14 nm, indicating the balanced reducibility (Fig. 2A). After 500 °C, the C peak appeared at 2θ of 26°, while Ni^0 peaks became significantly sharper, indicating a crystallite growth to 22 nm, related to the high surface energy of its smaller initial particles. After 600 °C, the phase composition of the system showed minimal changes compared to 500 °C, with a slightly more

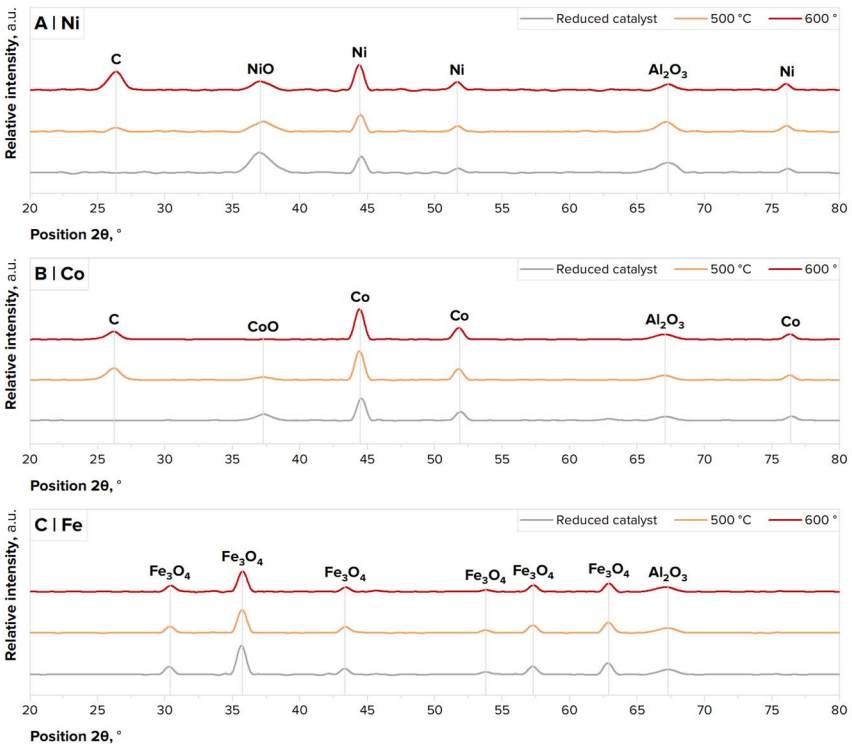

Fig. 11 XRD patterns for Ni/γ-Al_2O_3 (A), Co/γ-Al_2O_3 (B), and Fe/γ-Al_2O_3 (C) after reduction and the catalytic measurements at 500 °C and 600 °C.

Table 8 Crystallite sizes of the active phase metal particles for the studied catalytic systems after reduction and the catalytic measurements at 500 °C and 600 °C

	Crystallite size, nm		
Sample	Reduced catalysts	500 °C	600 °C
Ni/γ-Al_2O_3	14	22	23
Co/γ-Al_2O_3	19	25	26
Fe/γ-Al_2O_3	26	32	37

intense C peak, matching the increased carbon deposition (18.8% w/w at 500 °C and 21.7% w/w at 600 °C, Fig. 8), as well as a constant sharpness of Ni^0 peaks, suggesting the structural quasi-equilibrium of Ni crystallite size of 23 nm.[16,62,63] The growth in the size of Ni crystallites from 14 nm after reduction to 22–23 nm after the catalytic measurements is consistent with the tip-growth mechanism of carbon formation proposed on the basis of O_2–TPO and Raman spectroscopy (Fig. 9 and 10), whereby metallic Ni particles detach from the support surface and migrate towards the growing ends of carbon filaments, leading to particle coalescence and an apparent increase in crystallite size.[39,64]

The Co/γ-Al_2O_3 pattern (Fig. 11B) after reduction revealed Co^0 peaks at 2θ of 44°, 52°, and 76°, CoO at 2θ of 37°, γ-Al_2O_3 at 2θ of 67°, as well as an intermediate crystallite size of 19 nm, reflecting its dual reduction characteristics (Fig. 1B). After 500 °C, the catalyst exhibited a pattern similar to Ni/γ-Al_2O_3 with the new C peak at 2θ of 26°, as well as a relative intensification of the Co^0 peaks, demonstrating a further moderate growth in crystallite size to 25 nm. After 600 °C, the diffractogram, as in the case of Ni/γ-Al_2O_3, showed only minor changes – a growth of the intensity of the C peak, in line with the increase in carbon content (22.3% w/w at 500 °C and 24.3% w/w at 600 °C, Fig. 8), and virtually unvaried Co^0 peaks, emphasising the robustness of the Co active phase and the structural constancy of Co crystallites with a negligible increase to 26 nm, consistent with its in-between initial size and improved sintering resistance,

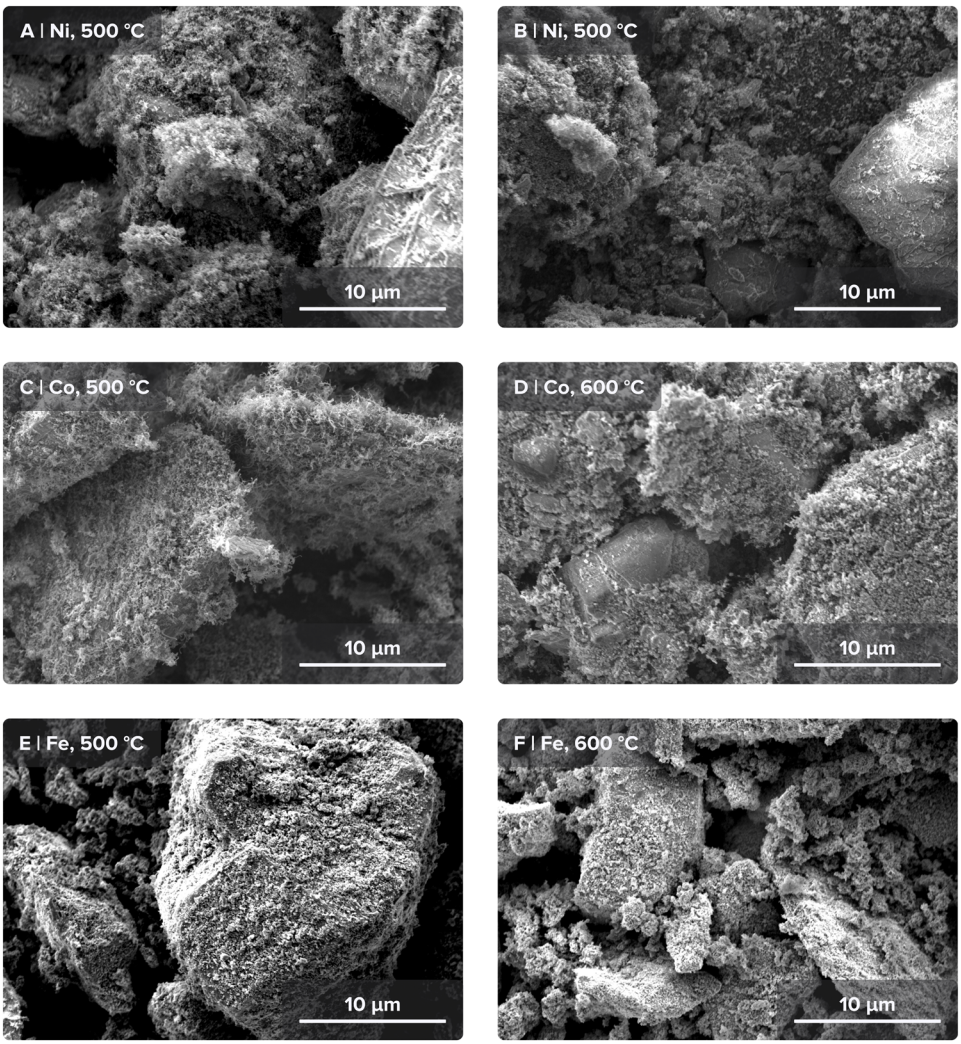

Fig. 12 SEM-EDX images of the samples after the catalytic measurements: Ni/γ-Al_2O_3 after 500 °C (A) and 600 °C (B); Co/γ-Al_2O_3 after 500 °C (C) and 600 °C (D); Fe/γ-Al_2O_3 after 500 °C (E) and 600 °C (F).

resulting from its distinct redox behaviour.[34,62] The more moderate increase in the size of Co crystallite compared to Ni, combined with the retention of Co^0 phase integrity after the catalytic measurements, is consistent with the carbon formation mechanism governed by the surface diffusion inferred from O_2-TPO and Raman spectroscopy (Fig. 9 and 10), wherein Co particles remain anchored to the support and do not undergo the substantial migration associated with the tip-growth pathway observed for Ni/γ-Al_2O_3.

The Fe/γ-Al_2O_3 catalyst (Fig. 11C) after reduction showed a complex oxide phase composition, characterised by peaks of Fe_3O_4 at 2θ of 30°, 36°, 43°, 54°, 57°, and 63°, γ-Al_2O_3 at 2θ of 67°, along with the largest initial crystallites of 26 nm owing to agglomeration propensity of Fe species due to low surface energy.[24] After both 500 °C and 600 °C, the diffractogram remain virtually unchanged, with no emergence of the C peak at an assumed 2θ of 26°, confirming the complete absence of carbon formation (Fig. 8 and 9) caused by the predominantly oxidised state of the catalyst (*ca.* 20% of reduced Fe^0 species, Fig. 4), as well as the continued growth of crystallite size to 32 nm at 500 °C and 37 nm at 600 °C, implying ongoing sintering driven by enhanced reduction above 550 °C, which increases the availability of mobile Fe^0 species.[65]

Surface structure and morphology. The results of SEM–EDX analysis of the carbon allotropes formed over the studied catalytic systems after the catalytic measurements at 500 °C and 600 °C are given in Fig. 12.

Ni/γ-Al_2O_3 after 500 °C (Fig. 12A) revealed a heterogeneous filamentous carbon morphology – thick, twisted thread-like structures extending from the catalyst particles and forming intertwined networks, with metal particles visible at the filament tips. This morphology serves as direct visual confirmation of the tip-growth mechanism, which was previously inferred from *ca.* 70% of reduced Ni^0 species according to *in situ* XPS (Fig. 2), the oxidation peak **Cγ** in O_2-TPO (Fig. 9), the gradual decrease in the Raman I_D/I_G ratio (Table 6), and the growth of Ni crystallite size from 14 to 22–23 nm established by XRD (Table 8 and Fig. 11A).[39,64] After 600 °C (Fig. 12B), the carbon morphology evolves into a more compact and agglomerated structure, retaining its filamentous character and increasing particle density. Such evolution indicated enhanced ordering and surface compaction, consistent with a significant decrease in the Raman I_D/I_G ratio (from 0.80 at 500 °C to 0.41 at 600 °C, Table 6), suggesting greater graphitisation, as well as a sharpening of the oxidation peak **Cγ** at 600 °C, attributed to the filamentous carbon (Fig. 9).

Co/γ-Al_2O_3 after 500 °C (Fig. 12C) displayed a markedly different morphology – dense, uniform 'carpet-like' carbon layers with fine, interwoven filaments forming a cohesive coating over the catalyst surface, with no visible metal particles at the ends of the filament. This morphology provides direct visual confirmation of the carbon growth mechanism *via* surface diffusion, which has previously been suggested from the stronger metal-support interaction established by H_2-TPR (peak **δ**, Fig. 1B) and *in situ* XPS (Fig. 5B), the smaller size of Co^0 crystallites after reduction of 6 nm (Fig. 5B), the high-temperature oxidation peak $\mathbf{C_\delta}$ in O_2–TPO (Fig. 9), the temperature-independent Raman I_D/I_G ratio (Table 6), and the moderate growth of Co crystallites from 19 to 25–26 nm in XRD (Table 8, Fig. 11B).[34,64]

Fe/γ-Al_2O_3 after both 500 °C and 600 °C (Fig. 12E and F) demonstrated no evidence of carbon deposition, showing only clean and structurally intact catalyst particles. The surface roughness and fragmentation at 600 °C are likely caused by thermal stress rather than carbon-related restructuring. The pristine surface provides visual confirmation of zero carbon formation, completely agreeing with the TOC and O_2-TPO (Fig. 8 and 9) analyses, which also showed a total absence of carbon deposition over this system. As mentioned earlier, this behaviour of Fe/γ-Al_2O_3 is directly attributed to the incomplete reduction of the catalyst (*ca.* 20% of metallic Fe^0 species, Fig. 4), induced by the prevalence of difficult-to-reduce Fe oxide and aluminate phases (peak δ with *ca.* 91% of peak area, Fig. 1C and 5C).

The convergence of the results obtained using all characterisation techniques employed has enabled the formulation of a self-consistent mechanistic picture, where the reducibility of the metal is the primary determinant of both catalytic activity and the pathway of carbon growth. The higher reducibility and moderate metal-support interaction over Ni/γ-Al_2O_3 favour the tip-growth mechanism *via* dissolution-precipitation, resulting in the formation of filamentous carbon with temperature-dependent graphitisation, as confirmed sequentially by O_2-TPO, Raman spectroscopy, XRD, and SEM-EDX. The stronger metal-support interaction and smaller metallic particle size over Co/γ-Al_2O_3 redirect carbon growth towards a surface diffusion-controlled pathway, producing inherently graphitic deposits, as confirmed by the same suite of techniques. The near-complete absence of metallic Fe^0 sites over Fe/γ-Al_2O_3 suppresses both pathways entirely, as confirmed by the absence of any carbon signal across TOC, O_2-TPO, Raman spectroscopy, XRD, and SEM–EDX.

Experimental section

Materials and reagents

Gamma-phase aluminium oxide (γ-Al_2O_3) by Chempur (Poland) was used as the support material. Nickel(II) nitrate hexahydrate ($Ni(NO_3)_2 \cdot 6H_2O$), cobalt(II) nitrate hexahydrate ($Co(NO_3)_2 \cdot 6H_2O$), and iron(III) nitrate nonahydrate ($Fe(NO_3)_3 \cdot 9H_2O$) by Chempur (Poland) were used as the active phase precursors. 99% ethanol (EtOH) by Chempur (Poland) was used as the impregnation medium.

25% v/v methane and 25% v/v carbon dioxide in argon mixture (25% CH_4 – 25% CO_2/Ar) by Linde (Poland) was used as the reaction gas mixture. 5% hydrogen in argon mixture (5% H_2/Ar) by Linde (Poland) was used as the reduction gas mixture. High-purity argon (Ar 5.0) by Linde (Poland) was used as the inert gas.

Preparation of the catalytic systems

The catalytic systems were synthesised *via* the wet impregnation method. 0.043 mol of $Me_x(NO_3)_y$ was dissolved in 100 mL of

EtOH, followed by the addition of 0.196 mol of γ-Al_2O_3 under constant magnetic stirring at 300 rpm and kept at RT for 24 h. EtOH was removed from the formed suspension using a rotary evaporator at 60 °C, 300 rpm. The resulting catalytic powder was calcined in a muffle furnace at 500 °C for 4 h. The obtained systems, containing 20% of the active phase, were designated as Me/γ-Al_2O_3 (*Me* = Ni, Co, Fe).

Analytical and experimental techniques

Characterisation of the catalytic systems. The active phase content was determined by atomic adsorption spectroscopy (AAS) using an Analytic Jena contrAA 300 spectrometer (Germany). A 0.02 g sample was mineralised in Teflon vessels with 8 mL LeFort's mixture (65% HNO_3 : 30% HCl = 3 : 1) using an Anton Paar Multiwave 3000 microwave system (Austria) at a microwave power of 1200 W, increased for 10 min, held for 15 min, and cooled for 15 min. Measurements were performed at characteristic wavelengths: 232.0 nm (Ni), 240.7 nm (Co), and 248.3 nm (Fe).

The textural properties (specific surface area, total pore volume, and average pore diameter) were analysed by Brunauer–Emmett–Teller (BET) and Barret–Joyner–Halenda (BJH) analyses using a Micrometrics AutoChem II + instrument (Canada). A 0.2 g sample was pretreated at a temperature of 25–350 °C at a rate of 50 °C min^{-1} for 10 min under He 5.0 flow at a rate of 50 mL min^{-1}, followed by cooling to RT. The physisorption of N_2 was performed using 26% N_2/He at a rate of 50 mL min^{-1} by cooling the reactor to −190 °C using a cryogenic bath (LN_2) and then gradually heating to ambient temperature using a water bath. The specific surface area was determined by the multi-point BET method applied to the adsorption branch, whilst the total pore volume and average pore diameter were derived from the BJH analysis of the desorption branch of the N_2 adsorption–desorption isotherm.

The acid–base properties were explored by temperature-programmed desorption of ammonia and carbon dioxide (NH_3– and CO_2-TPD) using a Micrometrics AutoChem II + instrument (Canada). A 0.2 g sample was pretreated at a temperature of 25–600 °C at 30 °C min^{-1} for 60 min under He 5.0 flow at a rate of 25 mL min^{-1}, followed by cooling to 50 °C. The sorption of NH_3 and CO_2 was performed using NH_3 5.0 and CO_2 5.0 at a rate of 15 mL min^{-1} for 20 min. After removing weakly adsorbed species at 100 °C, desorption was performed at a temperature of 100–600 °C at 20 °C under He 5.0 flow at a rate of 25 mL min^{-1} using TCD detection.

The reducibility of the studied catalytic systems was examined by temperature-programmed reduction by hydrogen (H_2–TPR) using a Micrometrics AutoChem II + instrument (Canada). A 0.1 g sample was pretreated at a temperature of 25–300 °C at a rate of 20 °C min^{-1} for 20 min under Ar 5.0 flow at a rate of 10 mL min^{-1}, followed by cooling to 40 °C. The reduction was performed using 5% H_2/Ar at a rate of 50 mL min^{-1} at a temperature of 40–800 °C at a rate of 10 °C min^{-1} using TCD detection.

The surface reduction of the studied catalytic systems was investigated by *in situ* X-ray photoelectron spectroscopy (*in situ* XPS) using a Shimadzu Kratos AXIS Ultra spectrometer (Japan) with a monochromatic AlKα X-ray source with an excitation energy of 1486.6 eV. A 0.1 g sample was pretreated in a high-temperature reaction cell (Cat-Cell) at a temperature of 25–500 °C at a rate of 10 °C min^{-1} under Ar 5.0 flow. The reduction was performed using 5% H_2/Ar at a rate of 50 mL min^{-1} and a pressure of 1 bar for 2 h, followed by cooling to 25 °C.

The bulk reduction of the studied catalytic systems was studied by *in situ* X-ray diffraction (*in situ* XRD) using a PANalytical X'Pert Pro MPD diffractometer (UK) equipped with an Anton Paar XRK900 reactor chamber (Austria) with a CuKα radiation source at 1.5406 Å in Bragg–Brentano geometry. A 0.15 g ground sample was pretreated in a glass ceramic sample holder at a temperature of 25–500 °C at a rate of 10 °C min^{-1} under Ar 5.0 flow. The reduction was performed using 5% H_2/Ar at a rate of 50 mL min^{-1} for 2 h, followed by cooling to 25 °C, and scanned at 2θ angle of 10–80° with an exposure per step of 100 s.

Catalytic measurements. The catalytic measurements were conducted in a custom-designed vertical continuous flow reactor with a fixed catalyst bed of 0.50 g in the isothermal zone. Prior to each measurement, the catalytic system was *in situ* preliminarily reduced in the reduction gas atmosphere at a temperature of 500 °C for 150 min. The process was performed at two temperatures: 500 °C and 600 °C for 150 min. All gases used, *i.e.*, reduction mixture (5% H_2/Ar), inert gas (Ar 5.0), and reaction mixture (25% CH_4 – 25% CO_2/Ar), were supplied at a flow rate of 50 mL min^{-1}.

The conversion of reaction gases and the yield of syngas during the catalytic measurements were determined by gas chromatography with thermal conductivity detection (GC–TCD) using a Chromatron GCHF 18.3 gas chromatograph (Germany) for H_2 detection under Ar 5.0 flow (detector temperature of 120 °C, column temperature of 120 °C) and INCO 505 M gas chromatograph (Poland) for CH_4, CO_2, and CO detection under He 5.0 flow (detector temperature of 100 °C, column temperature of 65 °C).

The calculations of the conversions of CH_4 and CO_2 and the yields of CO and H_2 were performed on the basis of GC–TCD data, using Ar as an internal standard and pre-determined response factors from calibration. This method accounts for non-equimolar reactions without requiring outlet flow measurements. The complete equations and derivations are provided in the SI.

Characterisation of the products. The carbon content in the samples after the catalytic measurements was analysed by total organic carbon (TOC) analysis using a Shimadzu TOC-500 instrument (Japan) equipped with a Shimadzu SSM-500 solid sampling module (Japan). A 0.03 g sample was oxidised in a ceramic boat at a temperature of 25–900 °C under O_2 5.0 flow for 10 min.

The types of carbon in the samples after the catalytic measurements were identified by temperature-programmed oxidation by oxygen (O_2-TPO) in a custom-designed continuous flow reactor using a Hiden Analytical HPR20 mass spectrometer (UK). A 0.1 g sample was oxidised in a quartz glass tube at a temperature of 25–800 °C at a rate of 10 °C min^{-1} under 5%

O_2/Ar flow at a rate of 40 mL min^{-1}. CO_2 was monitored by mass spectroscopy at m/z of 32 (O_2) and 44 (CO_2) at a pressure of 1.5–2.0 $\times$ 10^{-3} mPa.

The carbon structure in the samples after the catalytic measurements was characterised by Raman spectroscopy (RS) using a Horiba Jobin Yvon T64000 dispersive Raman spectrometer (Japan) equipped with an Olympus B-40 confocal microscope (Japan) at an excitation wavelength of 514.5 nm and a spectral resolution of 0.5 cm^{-1}.

The calculations of the carbon balance were established using Ar as a reference gas, GC-TCD outlet compositions, and the deposited carbon mass determined from TOC analysis. Carbon balance closure and carbon deposition efficiency were defined accordingly. The complete equations and derivations are provided in the SI.

The phase composition and crystallinity were determined by X-ray diffraction (XRD) using a PANalytical X'Pert Pro MPD diffractometer (UK) with a CuKα radiation source at 1.5406 Å in Bragg–Brentano geometry. The sample was scanned at 2θ angle of 5–80° with a step of 0.0167° and an exposure per step of 30 s.

The morphology and surface characteristics were studied by scanning electron microscopy with energy-dispersive X-ray spectroscopy (SEM-EDX) using a Hirox HR 5000 (E) digital optical microscope (Japan) equipped with a motorised triple zoom high-range lens, with a ThermoFisher Scientific Phenom XL scanning electron microscope (USA) equipped with an energy-dispersive X-ray spectrometer and operating at an acceleration voltage of 5 kV.

Conclusions

The present study provides a comprehensive investigation of the influence of transition metal active phases (Ni, Co, and Fe) on γ-Al_2O_3-supported catalytic systems on catalytic activity and the formation of nanostructured allotropic forms of carbon during low-temperature dry reforming of methane (500 °C and 600 °C). Through complex characterisation and evaluation, clear trends were established between the physicochemical properties of the studied catalytic systems, their reducibility, and both catalytic activity and carbon formation mechanisms. The research demonstrates that metal reducibility governs catalytic activity, while metal-specific carbon growth mechanisms determine catalyst stability and the nature of the carbon allotropes formed.

Ni/γ-Al_2O_3 displayed excellent activity and stability at both temperatures with significant formation of filamentous carbon structures. The catalyst exhibited balanced reducibility: *ca.* 70% of Ni species were successfully reduced to metallic Ni^0, according to the *in situ* XPS results. Such modest reducibility ensures good catalytic activity with CH_4 conversion of 64% at 500 °C and 76% at 600 °C, while CO_2 conversion reached 44% and 62%, respectively. The catalyst showed remarkable stability with minimal deactivation, particularly at 600 °C, where CH_4 conversion remained at 63% after 150 min. Carbon formation was moderate (18.8% w/w at 500 °C and 21.7% w/w at 600 °C), with the carbon deposition efficiency of 5.8% at 500 °C and 6.9% at 600 °C, and consisted primarily of filamentous carbon structures formed *via* a tip-growth mechanism. The carbon products exhibited significant temperature-dependent graphitisation, with the Raman I_D/I_G ratio decreasing from 0.80 at 500 °C to 0.41 at 600 °C, suggesting enhanced structural order at higher temperatures.

Co/γ-Al_2O_3 revealed the highest overall catalytic activity and the greatest carbon deposition among the studied catalytic systems. The catalyst demonstrated enhanced reducibility: *ca.* 60% of Co species were reduced to metallic Co^0, attributed to the presence of easily reducible Co species, as evidenced by the H_2-TPR profile. This superior reducibility resulted in the highest initial activity with CH_4 conversion of 78% at 500 °C and 75% at 600 °C, as well as CO_2 conversion of 58% and 63%, respectively. Nevertheless, the catalyst showed progressive deactivation, especially at 600 °C, presumably owing to extensive carbon accumulation affecting the active site accessibility. Carbon formation was consistently the highest among all systems (22.3% w/w at 500 °C and 24.3% w/w at 600 °C), reaching carbon deposition efficiency of 7.1% at 500 °C and 8.0% at 600 °C, with carbon products exhibiting an inherently graphitic character regardless of temperature. The Raman I_D/I_G ratio remained persistently low (0.48 at both temperatures), and SEM–EDX analysis demonstrated a distinctive 'carpet-like' morphology formed through surface diffusion and nucleation mechanisms rather than dissolution–precipitation pathways. The high thermal stability of the formed carbon was confirmed by O_2–TPO analysis, showing oxidation peaks at 650–700 °C, characteristic of graphitic carbon structures.

Fe/γ-Al_2O_3 exhibited minimal catalytic activity and a complete absence of carbon formation under the studied conditions; within this comparative study, it served as the mechanistic reference system, thereby enabling a direct assessment of the role of metal centre accessibility on the behaviour of the active Ni/γ-Al_2O_3 and Co/γ-Al_2O_3. The catalyst showed severely limited reducibility: only *ca.* 20% of Fe species were reduced to metallic Fe^0, consistent with the *in situ* XPS data, while *ca.* 91% of Fe species existed as difficult-to-reduce Fe aluminates, as judged by the H_2-TPR results showing the dominant peak at 890 °C. This poor reducibility led to negligible catalytic activity, with CH_4 and CO_2 conversion of 4% and 5% at 500 °C and 8% and 9% at 600 °C, respectively. The observed minimal conversion likely reflected background thermal reactions rather than genuine catalytic activity. None of the analytical methods utilised (TOC, O_2-TPO, Raman spectroscopy, or SEM–EDX) detected carbon deposition, confirming that the absence of reduced metal sites completely suppressed both the carbon-forming side reactions and the primary DRM reaction. The inclusion of Fe/γ-Al_2O_3 as a near-inactive reference system has provided crucial mechanistic insights. Thus, the strict correlation between the degree of metal reduction and both catalytic activity and carbon deposition confirms that exposed metal surface sites are a necessary prerequisite for carbon nucleation in the low-temperature DRM process. The almost complete carbon balance closure further validates the quantitative analytical approach employed.

Overall, the findings provide valuable insights into the quantitative relationships between metal reducibility, active site

density, catalytic activity, and carbon formation, and demonstrate that the systematic comparison of catalysts spanning the entire reducibility range – from readily reducible Co and Ni to the largely irreducible Fe – is an effective experimental strategy for isolating the role of metallic surface sites in the low-temperature DRM. The results highlight the potential for tailoring the DRM process towards either the syngas production with minimal catalyst deactivation or the controlled synthesis of valuable nanostructured carbon allotropes through rational catalyst design.

Author contributions

A. K.: conceptualisation, data curation, formal analysis, investigation, methodology, visualisation, writing – original draft preparation, writing – review and editing. O. S.: conceptualisation, methodology, supervision, writing – review and editing. W. M.: data curation, formal analysis, investigation, methodology. J. B.: data curation, formal analysis, investigation, methodology. H. K.-P.: formal analysis, methodology. M. K.: data curation, formal analysis, investigation. Y. S.: data curation, formal analysis, investigation. T. M.: methodology, supervision, writing – review and editing.

All authors have read and agreed to the published version of the manuscript.

Conflicts of interest

The authors declare that they have no known competing financial interests or personal relationships that could have appeared to influence the work reported in this paper.

Data availability

The data supporting the findings of this study are provided within this article and its supplementary information (SI). Additional data are available from the corresponding author upon reasonable request. Supplementary information: detailed carbon balance data for each of the catalytic measurements, as well as the methodology used to calculate the reaction parameters (reactant conversion and product yield) and the carbon balance. See DOI: https://doi.org/10.1039/d5ra09618a.

Acknowledgements

This article was completed while the first author (A. K.) was a doctoral candidate at the Interdisciplinary Doctoral School at the Lodz University of Technology (Poland). The authors are grateful to Jakub Kubicki and Magdalena Nowosielska (Institute of General and Ecological Chemistry, Faculty of Chemistry, Lodz University of Technology) for performing the analytical studies and consultations.

Notes and references

1 A. Kaporov, O. Shtyka, R. Ciesielski, A. Kedziora, W. Maniukiewicz, M. Szynkowska-Jozwik, Y. Madeniyet and T. Maniecki, *Materials*, 2023, **16**, 3180.
2 M. Hassan Amin, *Progress in Petrochemical Science*, 2018, **2**, DOI: 10.31031/PPS.2018.02.000532.
3 C. Jensen and M. S. Duyar, *Energy Technol.*, 2021, **9**, 2100106.
4 S. Arora and R. Prasad, *RSC Adv.*, 2016, **6**, 108668–108688.
5 M. Seemann and H. Thunman, in *Substitute Natural Gas from Waste*, Elsevier, 2019, pp. 221–243.
6 C. O. Calgaro and O. W. Perez-Lopez, *Mater. Chem. Phys.*, 2019, **226**, 6–19.
7 R. Colombo, G. Moroni, C. Negri, G. Delen, M. Monai, A. Donazzi, B. M. Weckhuysen and M. Maestri, *Angew. Chem., Int. Ed.*, 2024, **63**, e202408668.
8 K. Nagaoka, K. Seshan, K. Aika and J. A. Lercher, *J. Catal.*, 2001, **197**, 34–42.
9 J. R. Rostrup-Nielsen, *Catal. Today*, 1997, **37**, 225–232.
10 F. Sharifianjazi, A. Esmaeilkhanian, L. Bazli, S. Eskandarinezhad, S. Khaksar, P. Shafiee, M. Yusuf, B. Abdullah, P. Salahshour and F. Sadeghi, *Int. J. Hydrogen Energy*, 2022, **47**, 42213–42233.
11 M. Kogler, E.-M. Köck, B. Klötzer, T. Schachinger, W. Wallisch, R. Henn, C. W. Huck, C. Hejny and S. Penner, *J. Phys. Chem. C*, 2016, **120**, 1795–1807.
12 T. P. Maniecki, K. Bawolak, P. Mierczyński and W. K. Jozwiak, *Catal. Lett.*, 2009, **128**, 401–404.
13 L. M. Manocha, in *Encyclopedia of Materials: Metals and Alloys*, Elsevier, 2022, pp. 394–419.
14 F. Choudhary, P. Mudgal, A. Parvez, P. Sharma and H. Farooqi, *Nano-Struct. Nano-Objects*, 2024, **38**, 101186.
15 L. Wu, X. Xie, H. Ren and X. Gao, *Mater. Today: Proc.*, 2021, **42**, 153–160.
16 G. Li, H. Hao, P. Jin, M. Wang, Y. Yu and C. Zhang, *Fuel*, 2024, **362**, 130855.
17 E. Smal, Y. Bespalko, M. Arapova, V. Fedorova, K. Valeev, N. Eremeev, E. Sadovskaya, T. Krieger, T. Glazneva, V. Sadykov and M. Simonov, *Nanomaterials*, 2022, **12**, 3676.
18 E. Ruckenstein and H. Y. Wang, *J. Catal.*, 2002, **205**, 289–293.
19 T. P. Braga, R. C. R. Santos, B. M. C. Sales, B. R. da Silva, A. N. Pinheiro, E. R. Leite and A. Valentini, *Chin. J. Catal.*, 2014, **35**, 514–523.
20 A. J. Al Abdulghani, J.-H. Park, S. M. Kozlov, D.-C. Kang, B. AlSabban, S. Pedireddy, A. Aguilar-Tapia, S. Ould-Chikh, J.-L. Hazemann, J.-M. Basset, L. Cavallo and K. Takanabe, *J. Catal.*, 2020, **392**, 126–134.
21 I.-W. Wang, D. A. Kutteri, B. Gao, H. Tian and J. Hu, *Energy Fuels*, 2019, **33**, 197–205.
22 O. U. Osazuwa and K. H. Ng, *Results Eng.*, 2025, **25**, 104328.
23 I. Alstrup, *J. Catal.*, 1988, **109**, 241–251.
24 A. M. Manabayeva, P. Mäki-Arvela, Z. Vajglová, M. Martinéz-Klimov, T. Tirri, T. S. Baizhumanova, V. P. Grigor'eva, M. Zhumabek, Y. A. Aubakirov, I. L. Simakova, D. Y. Murzin and S. A. Tungatarova, *Ind. Eng. Chem. Res.*, 2023, **62**, 11439–11455.

25 L. B. Avdeeva, T. V Reshetenko, Z. R. Ismagilov and V. A. Likholobov, *Appl. Catal., A*, 2002, **228**, 53–63.
26 L. Zhou, L. R. Enakonda, M. Harb, Y. Saih, A. Aguilar-Tapia, S. Ould-Chikh, J. Hazemann, J. Li, N. Wei, D. Gary, P. Del-Gallo and J.-M. Basset, *Appl. Catal., B*, 2017, **208**, 44–59.
27 D. Shen, M. Huo, L. Li, S. Lyu, J. Wang, X. Wang, Y. Zhang and J. Li, *Catal. Sci. Technol.*, 2020, **10**, 510–516.
28 A. Abdulrasheed, A. A. Jalil, Y. Gambo, M. Ibrahim, H. U. Hambali and M. Y. Shahul Hamid, *Renewable Sustainable Energy Rev.*, 2019, **108**, 175–193.
29 M. H. Thi Bach, N. T. Tran, T. N. Thi Tran, V. C. Nguyen and H. A. Thi Nguyen, *Int. J. Chem. Eng.*, 2021, **2021**, 1–9.
30 A. Al-Fatesh, K. Acharya, A. I. Osman, G. Almutairi, A. H. Fakeeha, A. E. Abasaeed, Y. A. Al-Baqmaa and R. Kumar, *Int. J. Chem. Eng.*, 2023, **2023**, 1–11.
31 S. Yu, Y. Hu, H. Cui, Z. Cheng and Z. Zhou, *Chem. Eng. Sci.*, 2021, **232**, 116379.
32 Z. Zhang, Y. Han, F.-S. Xiao, S. Qiu, L. Zhu, R. Wang, Y. Yu, Z. Zhang, B. Zou, Y. Wang, H. Sun, D. Zhao and Y. Wei, *J. Am. Chem. Soc.*, 2001, **123**, 5014–5021.
33 S. Charan Nayak, S. Sengupta and G. Deo, *ChemistrySelect*, 2024, **9**, e202304841.
34 C. Q. Pham, A. N. T. Cao, P. T. T. Phuong, L. K. Hoang Pham, T. T. Vi Tran, T. H. Trinh, D.-V. N. Vo, T. P. T. Bui and T. M. Nguyen, *J. Energy Inst.*, 2022, **105**, 314–322.
35 K. Jabbour, A. Saad, L. Inaty, A. Davidson, P. Massiani and N. El Hassan, *Int. J. Hydrogen Energy*, 2019, **44**, 14889–14907.
36 J. Zhang, H. Xu, X. Jin, Q. Ge and W. Li, *Appl. Catal., A*, 2005, **290**, 87–96.
37 L. He, Y. Ren, B. Yue, S. C. E. Tsang and H. He, *Processes*, 2021, **9**, 706.
38 T. Ratana, S. Jadsadajerm, S. Tungkamani, W. Sumarasingha and M. Phongaksorn, *J. Phys. Chem. Solids*, 2024, **191**, 112034.
39 M.-J. Kim, J. Kim, Y. J. Kim, J.-R. Youn, D. H. Kim, D. Shapiro, J. Guo and K. Lee, *J. CO2 Util.*, 2024, **81**, 102721.
40 A. Zhao, W. Ying, H. Zhang, H. Ma and D. Fang, *Catal. Commun.*, 2012, **17**, 34–38.
41 V. R. Bach, A. C. de Camargo, T. L. de Souza, L. Cardozo-Filho and H. J. Alves, *Int. J. Hydrogen Energy*, 2020, **45**, 5252–5263.
42 J. L. Ewbank, L. Kovarik, C. C. Kenvin and C. Sievers, *Green Chem.*, 2014, **16**, 885–896.
43 É. Horváth, K. Baán, E. Varga, A. Oszkó, Á. Vágó, M. Törő and A. Erdőhelyi, *Catal. Today*, 2017, **281**, 233–240.
44 P. Arnoldy, J. L. De Booys, B. Scheffer and J. A. Moulijn, *J. Catal.*, 1985, **96**, 122–138.
45 A. S. Al-Fatesh, J. K. Abu-Dahrieh, H. Atia, U. Armbruster, A. A. Ibrahim, W. U. Khan, A. E. Abasaeed and A. H. Fakeeha, *Int. J. Hydrogen Energy*, 2019, **44**, 21546–21558.
46 N. Bayat, M. Rezaei and F. Meshkani, *Int. J. Hydrogen Energy*, 2016, **41**, 1574–1584.
47 H. W. Nesbitt, D. Legrand and G. M. Bancroft, *Phys. Chem. Miner.*, 2000, **27**, 357–366.
48 D. M. Guzman-Bucio, G. Gomez-Sosa, D. Cabrera-German, J. A. Torres-Ochoa, M. Bravo-Sanchez, O. Cortazar-Martinez, A. J. Carmona-Carmona and A. Herrera-Gomez, *J. Electron Spectrosc. Relat. Phenom.*, 2023, **262**, 147284.
49 C. A. Schwengber, F. A. da Silva, R. A. Schaffner, N. R. C. Fernandes-Machado, R. J. Ferracin, V. R. Bach and H. J. Alves, *J. Environ. Chem. Eng.*, 2016, **4**, 3688–3695.
50 A. R. Naghash, T. H. Etsell and S. Xu, *Chem. Mater.*, 2006, **18**, 2480–2488.
51 H. Kierzkowska-Pawlak, J. Tyczkowski, J. Balcerzak and P. Tracz, *Catal. Today*, 2019, **337**, 162–170.
52 X. Duan, M. Pan, F. Yu and D. Yuan, *J. Alloys Compd.*, 2011, **509**, 1079–1083.
53 M. D. Argyle, *Commemorative Issue in Honor of Professor Emeritus Calvin H. Bartholomew in Anticipation of His 75th Birthday*, MDPI, 2019.
54 X. Gao, Z. Ge, G. Zhu, Z. Wang, J. Ashok and S. Kawi, *Catalysts*, 2021, **11**, 1003.
55 M. J. Moradi and G. Moradi, *Int. J. Chem. React. Eng.*, 2024, **22**, 759–772.
56 M. Zhu, Y. Song, S. Chen, M. Li, L. Zhang and W. Xiang, *Chem. Eng. J.*, 2019, **368**, 812–823.
57 R. Babakouhi, S. M. Alavi, M. Rezaei, F. Jokar, M. Varbar and E. Akbari, *Int. J. Hydrogen Energy*, 2024, **60**, 503–514.
58 D. H. Le Phuong, M. Alsaiari, C. Q. Pham, N. H. Hieu, T.-P. T. Pham, N. Rajamohan, D. D. Pham, D.-V. N. Vo, T. H. Trinh, H. D. Setiabudi, D. L. T. Nguyen and T. M. Nguyen, *J. Taiwan Inst. Chem. Eng.*, 2024, **155**, 105253.
59 N. T. Tran, P. S. Kumar, Q. Van Le, N. Van Cuong, P. T. T. Phuong, A. A. Jalil, G. Sharma, A. Kumar, A. Sharma, B. V. Ayodele, S. Z. Abidin and D.-V. N. Vo, *Top. Catal.*, 2021, **64**, 338–347.
60 X. Liu, L. Zhang, X. Zheng, Y. Zhang, D. He and Y. Luo, *Int. J. Hydrogen Energy*, 2022, **47**, 30937–30949.
61 K. Selvarajah, N. H. H. Phuc, B. Abdullah, F. Alenazey and D.-V. N. Vo, *Res. Chem. Intermed.*, 2016, **42**, 269–288.
62 F. Rahbar Shamskar, M. Rezaei and F. Meshkani, *Int. J. Hydrogen Energy*, 2017, **42**, 4155–4164.
63 R. Rezaei and G. Moradi, *Int. J. Hydrogen Energy*, 2018, **43**, 21374–21385.
64 R. T. K. Baker, *Carbon*, 1989, **27**, 315–323.
65 K. J. Chaudhary, A. S. Al-Fatesh, A. A. Ibrahim, A. I. Osman, A. H. Fakeeha, M. Alhoshan, N. Alarifi, A. H. Al-Muhtaseb and R. Kumar, *Energy Convers. Manage.:X*, 2024, **23**, 100631.